Available online at www.CivileJournal.org

Civil Engineering Journal

(E-ISSN: 2476-3055; ISSN: 2676-6957)

Vol. 12, No. 04, April, 2026

Energy-Based Evaluation of Brittleness in Moderately Weathered Rocks Under Triaxial Compression

Lianghong Lv [1], Enze Yin [2*], Xiaoyu Liu [2], Ke Wu [2]

[1] *Guangdong Nanyue Transportation Investment and Construction Co., Ltd., Guangzhou 510100, China.*

[2] *School of Civil Engineering, Shandong University, Jinan 250021, China.*

Received 17 December 2025; Revised 09 March 2026; Accepted 16 March 2026; Published 01 April 2026

Abstract

Moderately weathered rock masses are widely encountered in deep and long tunnels, where excavation-induced unloading–reloading and stress concentration strongly affect failure behavior, stability, and support design. To clarify their brittleness from an energy perspective, this study develops a unified three-dimensional numerical framework for the triaxial compression analysis of five typical moderately weathered rocks, namely granite, basalt, limestone, shale, and sandstone, with the Jinmen Tunnel of the Longchuan–Huaiji Expressway as the engineering background. A coupled damage–plasticity constitutive model is adopted, and its parameters are calibrated using laboratory triaxial test data. Model reliability is verified by the close agreement between simulated and measured stress–strain curves and failure patterns of moderately weathered granite. The external work is decomposed into total, elastic, and dissipated energy densities, and a normalized dissipated energy is introduced to describe damage evolution. Results show that the energy evolution is strongly lithology-dependent: granite and shale exhibit a clear transition to post-peak dissipation-dominated behavior, whereas basalt, limestone, and sandstone remain mainly controlled by elastic energy. Increasing confining pressure from 5 to 10 MPa expands the dissipation zone and reduces the energy-density brittleness index B_{ED}, indicating a ductilizing effect. The novelty lies in the unified energy-based framework, the normalized dissipated energy, and the newly proposed B_{ED} for brittleness evaluation.

Keywords: Moderately Weathered Rock; Energy Dissipation; Damage–Plasticity Model; Brittleness Index; Confining Pressure; Triaxial Compression.

1. Introduction

Moderately weathered rock masses are widely encountered in long and deep tunnels such as the Jinmen Tunnel of the Longchuan–Huaiji Expressway, where excavation continuously disturbs the surrounding rock and induces repeated unloading–reloading cycles, local stress concentration, and alternating opening–closure of structural planes. Compared with fresh intact rock, moderately weathered rock usually contains abundant pre-existing microcracks, weakened cementation, altered minerals, and partially developed discontinuities, which make its deformation and failure behavior much more sensitive to excavation disturbance. In long tunnel construction, the rapid release of stored elastic energy, unstable crack coalescence, and brittle shear localization may directly threaten face stability, surrounding-rock safety, and support effectiveness. Therefore, a reliable brittleness evaluation of moderately weathered rocks is not only a theoretical issue in rock mechanics, but also a practical prerequisite for support design, excavation optimization, and construction risk control in complex tunnel engineering.

* Corresponding author: 202535179@mail.sdu.edu.cn

https://doi.org/10.28991/CEJ-2026-012-04-08

Existing studies on rock failure and brittleness can be broadly classified into three interrelated categories. The first category focuses on energy dissipation and damage evolution, and has established that rock deformation and failure are essentially governed by the accumulation, storage, release, transfer, and dissipation of energy under different stress paths. By examining the time evolution of incident, reflected, transmitted, and dissipated energies during dynamic impact failure, together with the associated strain responses of rock and support members, previous studies have clarified the energetic mechanisms of impact-induced damage in bolted rock systems and intact rock specimens [1, 2]. At the scale of underground openings, energy-based cavity-expansion analyses have further shown that the instability of the surrounding rock can be interpreted as a transition from a stable energy-storage state to an energy-driven failure state [3]. Under cyclic loading–unloading conditions, evolutionary models based on energy dissipation have been proposed to describe the progressive cracking and failure of coal and rock materials, revealing how energy accumulation mode, dissipation rate, and fracture development interact throughout the loading history [4]. For discontinuous geomaterials, constitutive descriptions of rock-joint hysteretic shearing have demonstrated that energy dissipation is negligible in the purely elastic stage but increases nonlinearly once sliding and irreversible damage are activated [5].

Triaxial cyclic loading and unloading tests on porous siltstone have further separated plastic dissipation energy from damage dissipation energy, thereby providing a more refined description of the staged evolution of crack growth, yielding, and failure localization [6]. Beyond conventional monotonic loading, recent studies have also shown that unloading paths, cyclic lower-limit effects, moisture variation, and confinement-dependent dilatancy all significantly affect the rate and mode of energy dissipation, and may even alter the dominant failure mechanism from tensile cracking to shear-expansion-controlled rupture [7-11]. Collectively, these studies demonstrate that energy evolution is not merely an accompanying phenomenon of failure, but a physically meaningful carrier of information on crack initiation, damage accumulation, localization, and macroscopic instability. The second category concerns the construction of brittleness criteria and brittleness indices, with the aim of transforming complex failure responses into quantitative descriptors that can distinguish brittle from ductile behavior. Early efforts in this direction improved the reliability of energy-related measurements by examining the influence of specimen geometry, loading configuration, and test quality on elastic, dissipated, and total energy components [12]. Other studies quantified dissipation factors under different deformation frequencies and rock origins, thereby extending the applicability of energy-based interpretation beyond standard compression tests [13]. At the theoretical level, critical energy threshold concepts have been proposed to interpret rock failure as the consequence of reaching an elastic energy limit modified by shear and dilation effects, providing a more general energetic criterion applicable from uniaxial to multiaxial stress states [14].

Building on such ideas, subsequent research has proposed differential strain-energy criteria, post-peak brittle-fracture point determination methods, brittleness models based on micro-damage evolution, full-strain comprehensive brittleness indices, and unified reviews of the applicability and limitations of existing brittleness indicators [15-18]. In addition, related studies on cemented or solidified geomaterials have incorporated elastoplastic pre-peak behavior and post-peak bearing-capacity attenuation into full-strain brittleness evaluation systems, thereby broadening the conceptual scope of brittleness quantification [19].

Hydro-mechanical coupling and long-term unloading effects have also been introduced into energy-based constitutive and evaluation frameworks, demonstrating that water content, time dependence, and confining-pressure unloading can strongly modify the coupling between energy dissipation, crack evolution, and apparent brittleness [20, 21]. These studies have greatly enriched the quantitative characterization of brittle–ductile transition, but they also suggest that many currently used indices still rely, either directly or indirectly, on the geometric features of stress–strain curves, and therefore may not fully capture the intrinsic balance between energy storage and energy dissipation. The third category involves damage–plasticity and thermodynamic constitutive modeling, which provides the theoretical and numerical basis for linking irreversible deformation, stiffness degradation, and energy conversion within a unified framework. Within a general thermodynamic formulation, the relationships among different dissipation mechanisms and intrinsic material behavior have been clearly established, and constitutive responses have been shown to depend on how different sources of dissipation contribute to the total energy budget [22].

On this basis, three-dimensional coupled damage–plasticity formulations with energy regularization have been developed to simulate fractured quasi-brittle rocks, explicitly distinguishing tensile and compressive damage processes and their corresponding dissipation characteristics [23]. Related constitutive approaches for creep and time-dependent failure have further introduced internal friction, dilatancy, and deformation-energy-based failure criteria into the modeling framework, making it possible to interpret long-term deformation and delayed instability from both mechanical and energetic perspectives [24]. Taken together, these modeling efforts have significantly improved the ability to reproduce nonlinear hardening, post-peak softening, strain localization, and progressive failure of quasi-brittle geomaterials under complex loading conditions. More importantly, they indicate that brittleness should not be viewed solely as a phenomenological feature of the stress–strain curve, but rather as the macroscopic manifestation of how a rock stores elastic energy before failure and how rapidly and intensively this stored energy is dissipated after peak loading.

Despite these important advances, several limitations remain. First, most previous studies focus on intact rocks or a single lithology, whereas a unified comparative analysis of multiple moderately weathered rocks under the same loading and modeling framework is still lacking. Second, many existing brittleness indices are still defined mainly from the geometric characteristics of stress–strain curves, and therefore do not directly reflect the physical competition between pre-peak elastic energy storage and post-peak energy dissipation, which is particularly important for moderately weathered rocks with strong crack compaction and progressive damage evolution. Third, from an engineering perspective, there is still insufficient research on energy-based brittleness classification for moderately weathered rocks under excavation environments in long tunnels, where unloading disturbance, confinement variation, and structural-plane activity jointly control deformation, failure mode, and support demand.

To address these gaps, this study conducts a systematic investigation into the triaxial compression behavior of five typical moderately weathered rocks—granite, basalt, limestone, shale, and sandstone—within a unified three-dimensional numerical framework. A coupled damage–plasticity constitutive model is adopted and calibrated using laboratory triaxial test results, and the external work is decomposed into total, elastic, and dissipated energy densities to reveal the energy evolution characteristics of different lithologies under different confining pressures. On this basis, a normalized dissipated energy is introduced to characterize damage development, and a new energy-density brittleness index B_{ED} is proposed to quantify the balance between pre-peak elastic energy accumulation and post-peak dissipation. The main contribution of this work is therefore to provide a unified energy-based framework for the brittleness comparison of multiple moderately weathered rocks and to offer a more physically grounded basis for excavation and support design in long tunnel engineering.

2. Engineering Background

The Jinmen Tunnel is the controlling project of the Longchuan–Huaiji Expressway in Guangdong Province, China, and is currently the longest highway tunnel in the province. It is located between Wangbu Town and Donghua Town in Yingde City, with a total length of 6492 m for the left bore and 6482.6 m for the right bore. The tunnel traverses the Huashuishan Nature Reserve, where the terrain is characterized by steep topographic relief and high environmental sensitivity, thereby imposing strict requirements on construction-disturbance control and surrounding-rock stability assessment. Along its alignment, the tunnel crosses two major geomorphic units: the low-to-middle mountainous area of Huashuishan and the Beijiang Basin. The mountainous section is generally higher in the east and lower in the west, with steep longitudinal gradients, deeply incised gullies, elevations ranging from 32 to 600 m, and well-developed surface vegetation. In contrast, the Beijiang Basin is dominated by fine-grained soils, including silty clay, secondary red clay, and silt, all of which exhibit high water-retention and saturation capacity. At the regional scale, the landforms are mainly classified as tectonic–denudational, erosional–accumulational, and erosional–tectonic, and the interaction between surface water and groundwater is particularly active.

Geologically, the tunnel crosses the Xueshanzhang anticline, where fractures are intensely developed and the rock mass within the axial zone is highly fragmented. The two limbs of the anticline are characterized by monoclinal structures, while local slip surfaces and dip slopes occur near the tunnel portals, posing potential stability risks during construction. According to the available engineering-geological data, the proportions of surrounding-rock classes are approximately 37.7% for Class III, 50.0% for Class IV, and 12.3% for Class V. Several key sections, including K198+454–K198+474, K199+114–K199+144, and K199+334–K199+374, intersect moderately weathered rock strata such as granite, basalt, limestone, shale, and sandstone, which are prone to local stress concentration. Under tunnel excavation disturbance, the surrounding rock is subjected to repeated unloading–reloading cycles, and the alternating opening and closure of structural planes become increasingly pronounced. This process accelerates volumetric deformation, damage accumulation, and local collapse, and may therefore act as a critical trigger for progressive or even cascading failure of the tunnel surrounding rock. Given that the Jinmen Tunnel passes through multiple moderately weathered rock sections with complex structural conditions and pronounced excavation-induced unloading effects, the use of graded confining pressures is more representative than adopting a single stress level for brittleness analysis. Such a setting makes it possible to capture the variation in rock response under different confinement environments associated with changes in burial depth, geological conditions, and local stress redistribution during tunnel excavation.

These geological features also provide a direct engineering rationale for the lithology selection adopted in this study. In particular, the key sections K198+454–K198+474, K199+114–K199+144, and K199+334–K199+374 intersect moderately weathered granite, basalt, limestone, shale, and sandstone, which are representative of the major lithological types encountered along the Jinmen Tunnel alignment. Under excavation disturbance, these moderately weathered rocks are especially susceptible to local stress concentration, repeated unloading–reloading effects, alternating opening and closure of structural planes, and progressive damage accumulation. As a result, their deformation and failure characteristics are expected to differ markedly in terms of energy storage, dissipation, and brittle instability. The selection of these five lithologies therefore has a clear engineering basis and is directly relevant to the assessment of surrounding-rock stability and support demand in the Jinmen Tunnel and similar long-tunnel projects.

3. Numerical Model and Methodology

3.1. Rock Types and Mechanical Parameters

Five representative lithologies were selected for this study: moderately weathered granite, shale, sandstone, limestone, and basalt. These rocks correspond to different major engineering lithological categories and collectively cover several of the most common rock groups encountered in underground construction, including igneous rocks, clastic sedimentary rocks, carbonate rocks, and fine-grained sedimentary rocks. More importantly, their selection is directly related to the geological conditions of the Jinmen Tunnel, where moderately weathered granite, basalt, limestone, shale, and sandstone are present in key sections along the alignment. From a mechanical perspective, these lithologies span a broad spectrum of deformation and failure characteristics, including relatively brittle rock types as well as more deformable ones. They therefore provide a suitable basis for a unified comparison of energy evolution, damage development, and brittleness under the same numerical framework. In the moderately weathered state, the original rock texture and structure generally remain identifiable, while joints, fissures, and mineral alteration become increasingly developed, resulting in a more complex mechanical response than that of fresh intact rock. For each lithology, the fundamental mechanical parameters were determined from laboratory triaxial tests and are summarized in Table 1, including the elastic modulus (E), Poisson's ratio (ν), cohesion (c), internal friction angle (ϕ), tensile strength (σ_t), and damage-related parameters. These parameters were subsequently used to calibrate the constitutive model adopted in the numerical simulations.

Table 1. Basic mechanical parameters of the five moderately weathered rocks

Rock type	Elastic modulus (E/GPa)	Poisson's ratio (ν)	Internal friction angle (φ/°)	Uniaxial compressive strength (σ_{uc}/MPa)	Tensile strength (σ_t/MPa)	Density (ρ/kg/m^3)
Moderately weathered granite	15	0.25	35	55	4.5	2600
Moderately weathered basalt	22	0.25	28	63	5	2755
Moderately weathered limestone	12	0.26	22	38	2.8	2400
Moderately weathered shale	8	0.28	18	24	1.8	2200
Moderately weathered sandstone	18	0.22	25	52	4.2	2550

3.2. Constitutive Model: Damage–Plasticity Formulation

To capture both plastic deformation and damage evolution in moderately weathered rocks, a coupled damage–plasticity model is adopted. The total strain tensor ε is decomposed into elastic and plastic parts:

$$\varepsilon = \varepsilon^e + \varepsilon^p \tag{1}$$

where ε denotes the total strain tensor, ε^e the elastic strain tensor, and ε^p the plastic strain tensor.

The effective stress $\tilde{\sigma}$ obeys an elastoplastic law, while the nominal stress σ is degraded by a scalar damage variable D ($0 < D < 1$):

$$\sigma = (1 - D)\,\tilde{\sigma} \tag{2}$$

The plastic behavior is described by a Drucker-Prager type yield function:

$$F = \alpha I_1 + \sqrt{J_2} - k = 0 \tag{3}$$

where I_1 is the first invariant of the effective stress tensor, J_2 is the second invariant of the deviatoric stress tensor, and α, k are material constants related to cohesion and internal friction angle. An associated or non-associated flow rule can be adopted depending on the lithology.

The damage variable D is taken as a function of an energy-based internal variable κ, which accumulates the dissipated energy density:

$$D = D(\kappa),\ \kappa = \int_0^{\varepsilon} \mathrm{d}\, U_{\mathrm{d}} \tag{4}$$

A typical exponential damage evolution law is used:

$$D = 1 - \exp\left(-\frac{\kappa}{\kappa_0}\right) \tag{5}$$

where κ_0 is a characteristic dissipated energy density controlling the damage rate. Different rocks have different κ_0 values to represent their distinct damage sensitivities.

3.3. Triaxial Specimen and Boundary Conditions

The numerical specimen was modeled as a right circular cylinder with a height-to-diameter ratio of 2:1, consistent with the standard configuration adopted in triaxial compression tests. To reduce computational cost, a one-eighth symmetric model was employed, and the corresponding symmetry boundary conditions were imposed on the relevant planes. Confining pressures σ_3 of 5, 10, and 15 MPa were applied to the lateral surface. In this study, these three pressure levels represent low confinement, intermediate confinement, and relatively high confinement, respectively, and are intended to simulate the range of confinement states that may occur in long tunnels under different burial depths and excavation-disturbance-induced stress redistribution conditions. Figure 1 presents the basic workflow adopted in this study.

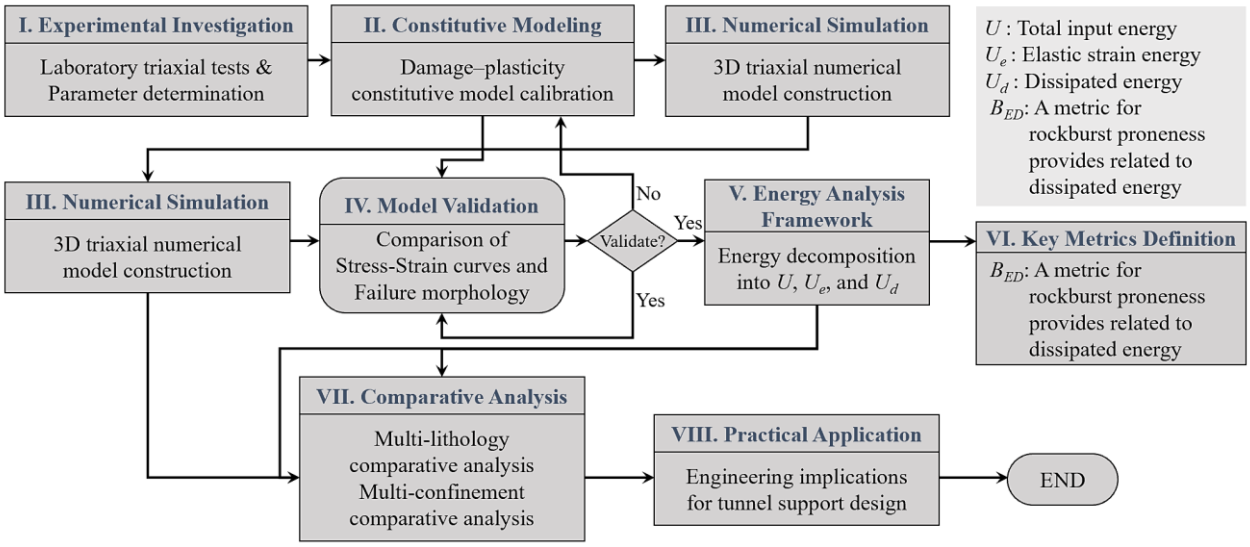

Figure 1. Research method flow chart

3.4. Parameter Calibration Procedure

The constitutive parameters were calibrated using an iterative regression-based fitting procedure constrained jointly by laboratory test results and numerical response. First, the initial elastic and strength parameters, including the elastic modulus E, Poisson's ratio ν, uniaxial compressive strength σ_{uc}, tensile strength σ_t, cohesion-related terms, and internal friction angle ϕ, were determined from the laboratory triaxial and mechanical test data summarized in Table 1. On this basis, the Drucker–Prager parameters α and k were obtained from the corresponding strength parameters to define the initial yield surface, while the damage-related parameter κ_0 and the associated softening parameters were assigned preliminary values according to the observed post-peak characteristics of each lithology. These parameters provided the initial constitutive input for the numerical simulations.

The subsequent calibration aimed to reproduce the main features of the experimental response, including the slope of the elastic segment, peak strength, peak strain, post-peak softening rate, and the overall failure morphology. Starting from the initial parameter set, the numerical stress–strain response was compared with the laboratory curves, and the constitutive parameters were adjusted step by step until a satisfactory agreement was achieved. In particular, the elastic constants mainly controlled the pre-peak stiffness, the plastic parameters governed the onset of yielding and peak strength, and the damage-related parameters controlled the post-peak degradation and dissipation characteristics. The fitting objective was to minimize the discrepancy between the simulated and experimental stress–strain curves while maintaining consistency with the observed fracture-dominated failure patterns. In the present study, moderately weathered granite was used as the representative lithology for direct calibration and validation because complete triaxial stress–strain and failure-pattern data were available for this rock type. The resulting calibrated model reproduced both the measured mechanical response and the macroscopic failure characteristics with good accuracy, thereby providing a reliable basis for the subsequent comparative analyses of the other moderately weathered lithologies.

3.5. Reliability Verification

A numerical model was established to simulate the triaxial compression behavior of rock based on the foregoing theoretical framework, and its reliability was validated against laboratory data obtained from the SANS-500C rock triaxial testing system, as shown in Figure 2. Moderately weathered granite was selected as the representative material for model calibration and validation. Standard cylindrical specimens with dimensions of ϕ50 mm ×

100 mm were prepared. The specimen ends were carefully machined to ensure a parallelism deviation of less than 0.02 mm, thereby minimizing stress concentration induced by eccentric loading. To prevent direct contact between the confining fluid and the specimen, each sample was enclosed in a red silicone rubber sleeve, as illustrated in the right panel of Figure 2.

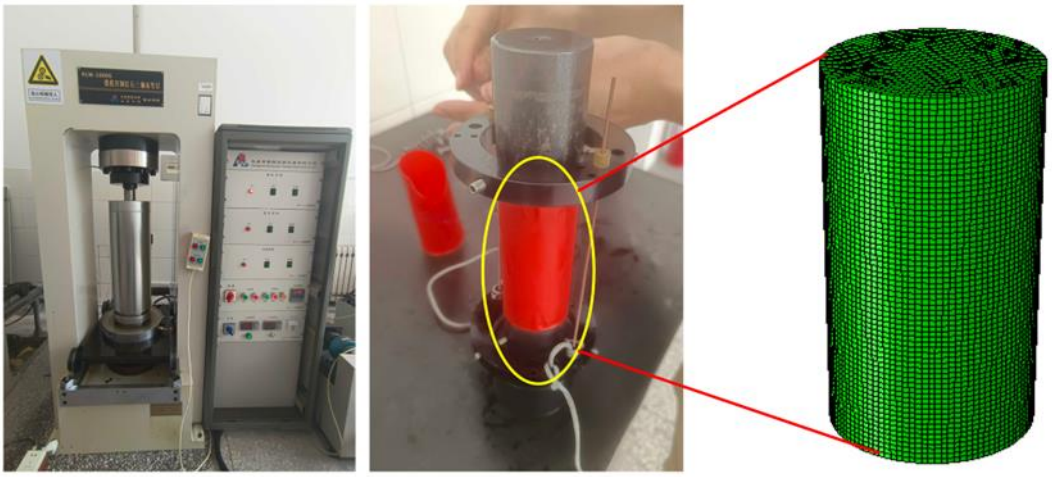

Figure 2. Triaxial compression test and numerical model of rock

Axial loading was applied through rigid upper and lower platens, while deformation and load responses were continuously recorded in real time using displacement gauges and pressure sensors. A constant confining pressure, typically 10 MPa, was maintained throughout the test. The loading procedure consisted of two stages. First, the target confining pressure was applied and stabilized via an automatic pressurization system. Second, under constant confining pressure, axial loading was imposed at a constant displacement rate (e.g., 0.002 mm/s) until specimen failure. After failure, selected specimens were sectioned and photographed to identify shear-band development and failure modes. The experimental data included axial stress, axial strain, volumetric strain, and failure morphology. The resulting stress–strain curves were used for constitutive calibration and parameter fitting, whereas the observed failure patterns provided additional evidence for assessing the model's capability to reproduce fracture-dominated failure behavior.

Figure 3 presents a comparison between the failure patterns observed in laboratory triaxial compression tests and those predicted numerically for moderately weathered granite. As shown in the figure, the numerical model agrees well with the experimental results in terms of both the macroscopic failure morphology and the orientation and propagation trend of the dominant fracture planes. This consistency indicates that the proposed model is capable of reliably capturing the principal deformation and failure characteristics of rock under triaxial loading conditions.

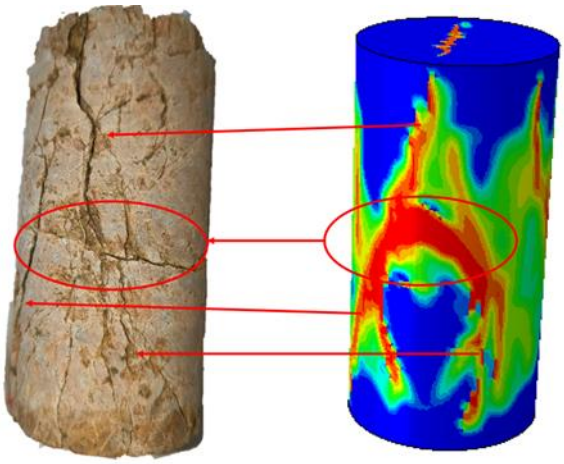

Figure 3. Comparison of measured and simulated failure patterns of indoor triaxial compression test rock samples

Figure 4 further compares the axial stress–strain curves obtained from the numerical simulation and the laboratory tests under a confining pressure of 10 MPa. The simulated results show good agreement with the experimental data, particularly with respect to peak strength, deformation evolution, and post-peak softening behavior. Overall, the close correspondence in both failure mode and mechanical response demonstrates the validity of the proposed numerical model for reproducing the triaxial compression behavior of moderately weathered granite.

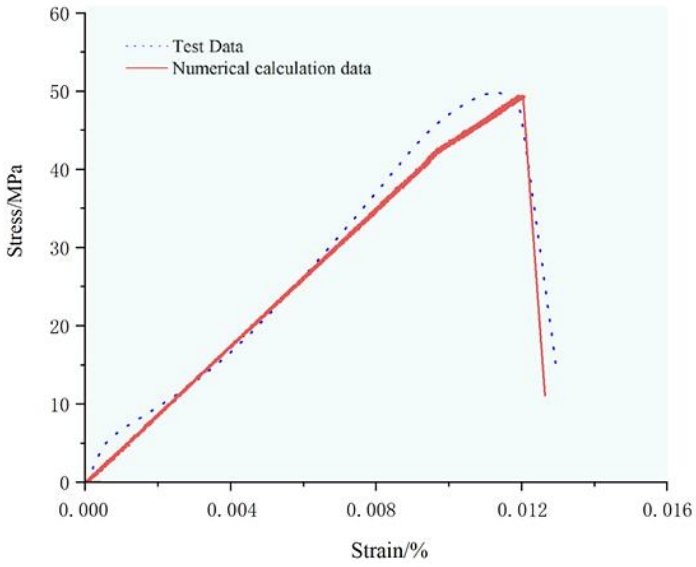

Figure 4. Comparison of Axial Stress-Strain Curves under a Confining Pressure of 10 MPa

In summary, the developed numerical model can realistically reproduce the deformation and failure behavior of rock under different confining pressures. It therefore provides a robust and reliable framework for investigating energy dissipation mechanisms and offers a sound basis for subsequent analyses of failure evolution and damage-related energy partitioning. Granite was used as the representative lithology for direct model validation because it had the most complete triaxial test dataset, including both stress–strain response and failure morphology.

3.6. Energy Decomposition and Definition of a New Brittleness Index

During triaxial compression, the work done by external loading is stored and dissipated inside the rock specimen in different forms. For a unit volume, the incremental external work can be written as:

$$\mathrm{d}U = \sigma : \mathrm{d}\varepsilon \tag{6}$$

where σ is the nominal stress tensor, ε is the total strain tensor, and ":" denotes the inner product of two tensors. The term $\mathrm{d}U$ represents the increase of total energy density within a small loading increment.

For a given axial strain ε_a, the accumulated input energy density from the initial state to this strain level is:

$$U(\varepsilon_a) = \int_0^{\varepsilon_a} \sigma : \mathrm{d}\varepsilon \tag{7}$$

This total energy can be decomposed into two parts: the recoverable elastic strain energy U_e and the irrecoverable dissipated energy U_d,

$$U = U_e + U_d \tag{8}$$

The elastic strain energy density is calculated from the current stress state and the elastic strain tensor ε^e as:

$$U_e = \frac{1}{2}\sigma : \varepsilon^e \tag{9}$$

Assuming that the material follows the generalized Hooke's law in the elastic regime. Accordingly, the dissipated energy density is obtained as:

$$U_d = U - U_e \tag{10}$$

which reflects the energy consumed by plastic deformation, microcrack initiation and propagation, frictional sliding, and other irreversible processes. The evolution of U_d with loading thus provides an energetic description of damage development and failure.

To enable a unified comparison among different lithologies and confining pressures, a normalized dissipated energy density is introduced:

$$\overline{U}_d(\varepsilon_a) = \frac{U_d(\varepsilon_a)}{U_d^{peak}} \tag{11}$$

where U_d^{peak} is the dissipated energy density at the peak deviatoric stress. By normalizing with respect to U_d^{peak}, the damage-evolution trajectories of different rocks are mapped into a common interval of 0-1, which filters out the differences in absolute energy levels and highlights the relative evolution pattern.

On the basis of this energy decomposition, a new energy-density brittleness index B_{ED} is proposed to quantify the balance between pre-peak energy storage and post-peak dissipation:

$$B_{ED} = \frac{U_e^{peak}}{U_e^{peak} + U_d^{post}} \quad (12)$$

where U_e^{peak} is the elastic strain energy density at the peak deviatoric stress, and U_d^{post} is the additional dissipated energy density accumulated from the peak strain to a prescribed post-peak strain level (for example, when the axial stress drops to 80% of the peak value). The physical meaning of B_{ED} can be interpreted as follows:

- A large B_{ED} indicates that the rock stores a considerable amount of elastic energy before failure, while only a relatively small additional dissipated energy is required in the post-peak stage, corresponding to a more brittle response;
- A small B_{ED} means that a significant portion of the external work has already been dissipated before the peak, and the post-peak process still needs to dissipate substantial energy to complete failure, corresponding to a more ductile or quasi-plastic behavior.

Therefore, B_{ED} directly links the conventional concepts of "brittleness" and "ductility" to the partition of stored and dissipated energies, providing a physically grounded and unified measure for evaluating the brittleness of moderately weathered rocks with different lithologies.

4. Results

4.1. Stress–Strain Behavior of Different Lithologies

Figure 5 shows the axial stress–strain responses of five moderately weathered rocks, namely granite, basalt, limestone, shale, and sandstone, under confining pressures of 5, 10, and 15 MPa. For all lithologies, the curves exhibit an initial approximately linear segment, followed by a nonlinear hardening stage toward a distinct peak, and then a pronounced post-peak softening branch, indicating a generally brittle failure pattern. Nevertheless, clear lithology-dependent differences can still be identified in both the pre-peak deformation capacity and the post-peak instability characteristics. In particular, shale exhibits the largest peak strain, reaching nearly 2% in some cases, whereas granite, basalt, and sandstone generally fail at much smaller axial strains. This higher deformability of shale can be attributed to its relatively weak cementation, more developed initial microcrack system, and stronger capacity for crack closure, frictional sliding, and local plastic accommodation during loading. As a result, shale is able to sustain a longer inelastic deformation stage before the onset of macroscopic instability. By contrast, basalt and sandstone display comparatively smaller peak strains and steeper post-peak stress drops, indicating stronger brittleness. For basalt, this behavior is likely associated with its relatively dense and stiff mineral skeleton, which allows substantial elastic energy accumulation but provides limited deformation accommodation once localized cracking initiates. For sandstone, the stress-bearing granular framework can also sustain considerable elastic loading prior to failure, but once intergranular cracking and shear localization develop, the residual load-carrying capacity degrades rapidly, leading to a brittle post-peak response. These features are consistent with the view that basalt and sandstone are dominated more strongly by elastic energy storage than by stable post-peak dissipation.

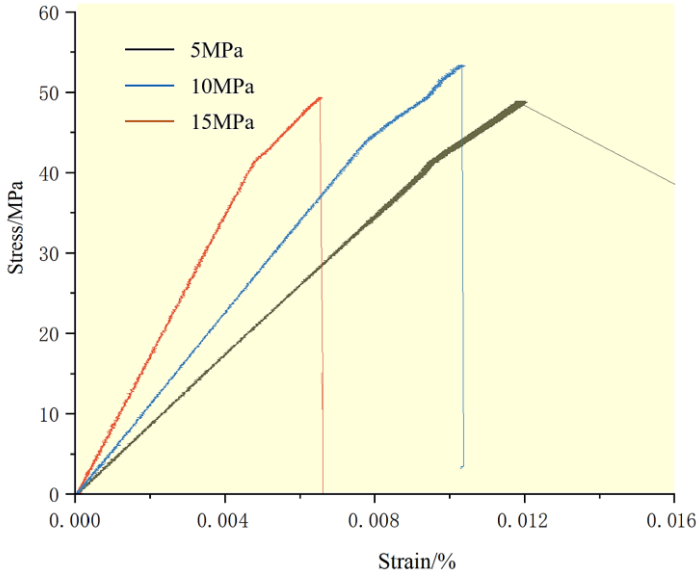

(a) Moderately weathered granite

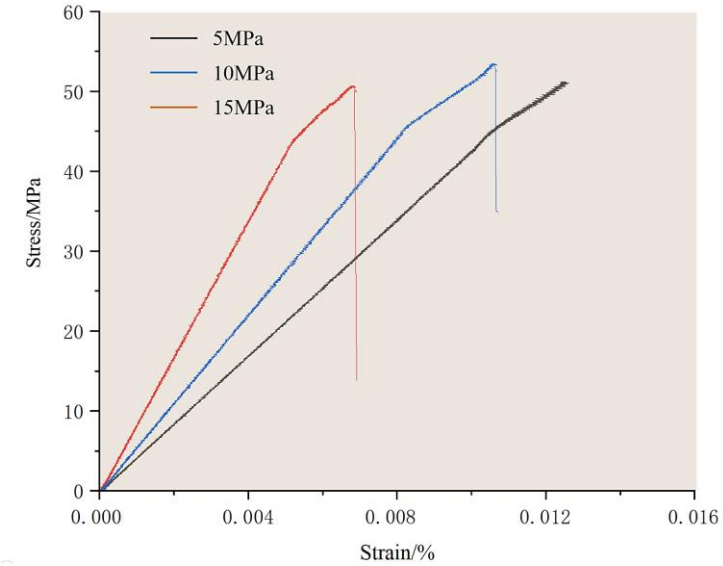

(b) Moderately weathered basalt

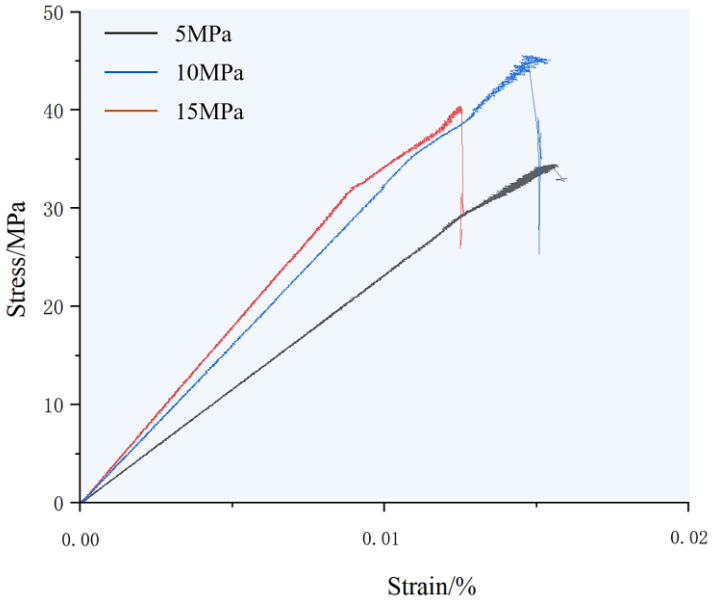

(c) Moderately weathered limestone

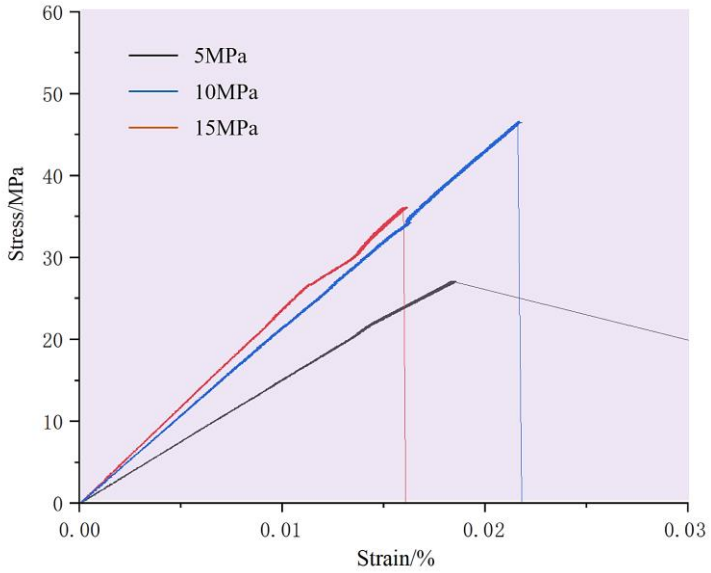

(d) Moderately weathered shale

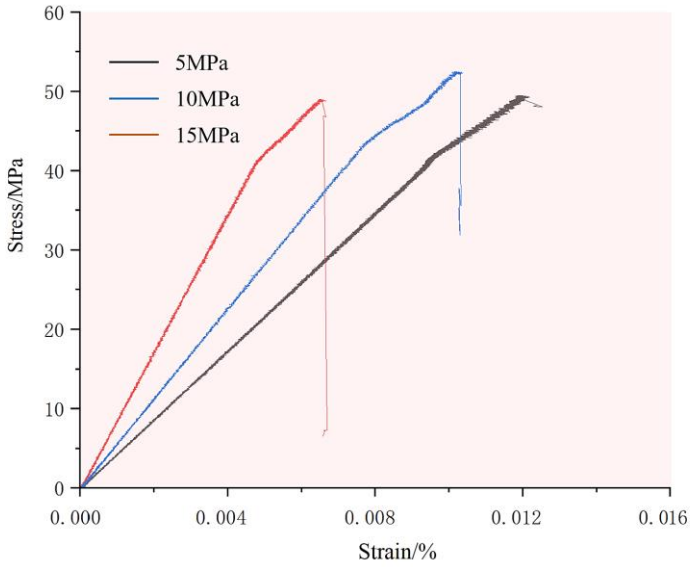

(e) Moderately weathered sandstone

Figure 5. Stress-strain curves of rock samples under different confinement pressures

A consistent strengthening effect of confinement is observed when the confining pressure increases from 5 to 10 MPa. For all lithologies, the peak strength increases and the peak strain shifts slightly to larger values, while the onset of post-peak instability is delayed. Mechanistically, the additional lateral confinement suppresses tensile crack opening, restrains dilatancy, and enhances frictional resistance along pre-existing flaws and newly formed microcracks. Consequently, a larger amount of external work is required before unstable crack coalescence and shear-band localization can occur, which explains why the hardening stage becomes longer and the macroscopic failure is postponed under higher confinement. In this sense, increasing confinement promotes a transition from immediate brittle rupture toward a relatively more stable deformation-and-dissipation process, even though the overall response remains brittle in a nominal stress–strain sense.

However, the responses under 15 MPa show a distinct non-monotonic deviation from the above trend, with lower peak strengths, smaller peak strains, and nearly vertical post-peak drops compared with the corresponding 10 MPa cases. This phenomenon should be interpreted with caution and should not be directly regarded as an intrinsic material law without further verification. From the perspective of model setting, the adopted coupled damage–plasticity formulation may adequately capture the behavior under low-to-moderate confinement, but its hardening, dilatancy, and damage-softening assumptions may become less accurate at higher confinement, especially if the constitutive parameters were calibrated mainly using a limited pressure range. From the perspective of the loading path, the numerical implementation of confining-pressure application and subsequent axial loading may influence the stability of the pre-peak and post-peak response; for example, an abrupt transition between loading stages or insufficiently smooth displacement control may artificially trigger premature instability near the peak. From the perspective of boundary conditions, platen restraint, end friction, stress non-uniformity, or confinement transmission effects may promote early shear localization from the specimen ends, thereby shortening the apparent deformability and reducing the computed peak strength. From the perspective of parameter calibration, the sensitivity of the damage variable, characteristic dissipated-energy threshold, and plastic-flow parameters at 15 MPa may not yet be fully constrained, such that the model could overpredict damage acceleration or underpredict confinement-induced hardening. Therefore, the anomalous 15 MPa response is more appropriately treated as a result that requires further calibration and validation, rather than as definitive evidence of a true strength reduction under increasing confinement.

4.2. Energy Evolution under Triaxial Loading

Figure 6 illustrates the spatial distribution of unit dissipated energy in the numerical specimens after triaxial failure for five moderately weathered rock types under confining pressures of 5, 10, and 15 MPa. For all lithologies, the yellow–red high-dissipation zones clearly delineate the dominant failure paths, confirming that the proposed energy-based formulation is capable of capturing the localization patterns associated with post-peak damage evolution. Under a low confining pressure of 5 MPa, dissipated energy is mainly concentrated within one or two narrow inclined bands, indicating highly focused strain localization and a relatively limited damage volume. This concentrated localization can be attributed to the weak lateral restraint under low confinement, which allows tensile wing-crack opening, rapid crack coalescence, and early formation of a dominant shear path. Once such a preferential failure plane is formed, subsequent deformation is strongly confined to that narrow zone, resulting in a sharp and localized dissipation pattern. As the

confining pressure increases to 10 and 15 MPa, the dissipation zone becomes markedly broader and more complex, often developing into intersecting or X-shaped shear bands. This widening of the damage region reflects the fact that higher confinement suppresses direct tensile opening and delays abrupt instability, so that more external work must be accommodated through distributed microcrack growth, frictional sliding, and progressive shear interaction before final failure occurs. Consequently, damage is no longer restricted to a single narrow band, but spreads over a larger volume of the specimen.

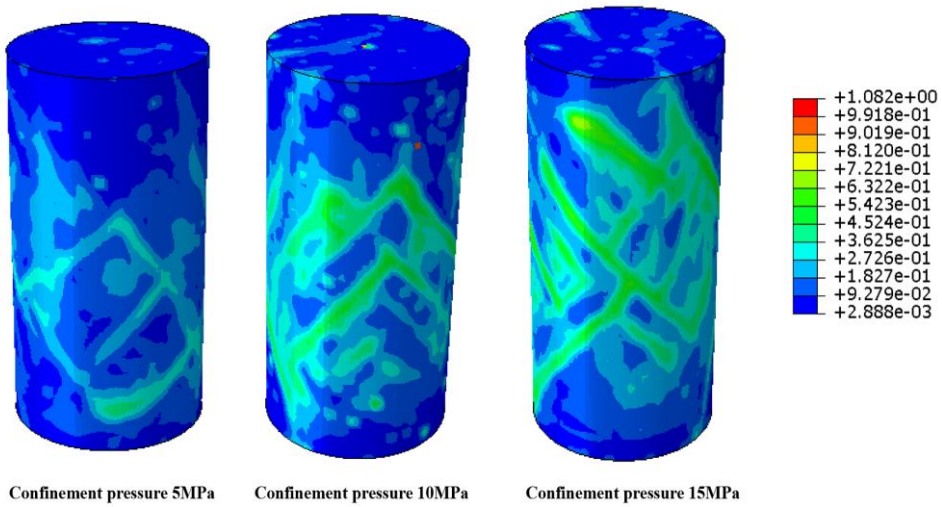

(a) Moderately weathered granite

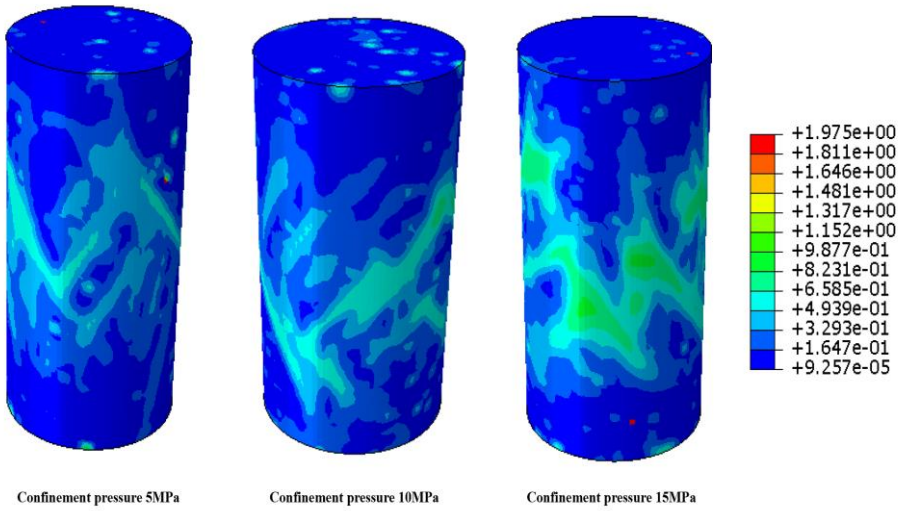

(b) Moderately weathered basalt

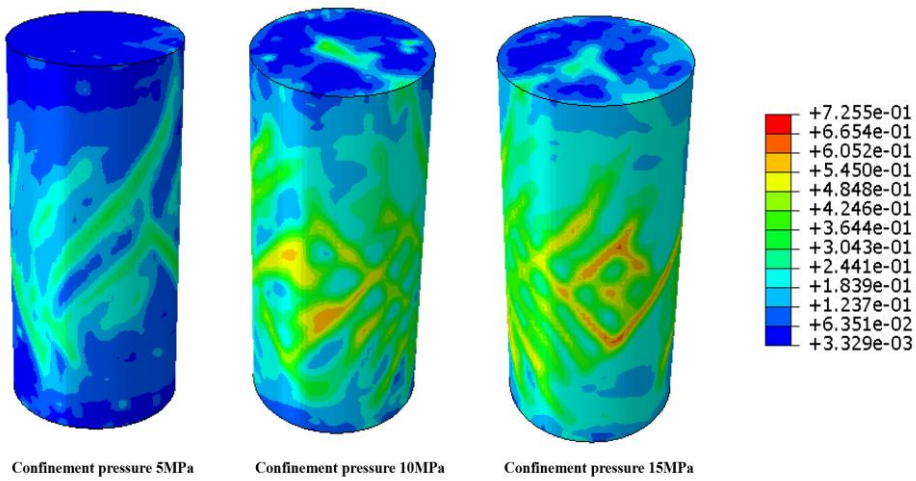

(c) Moderately weathered limestone

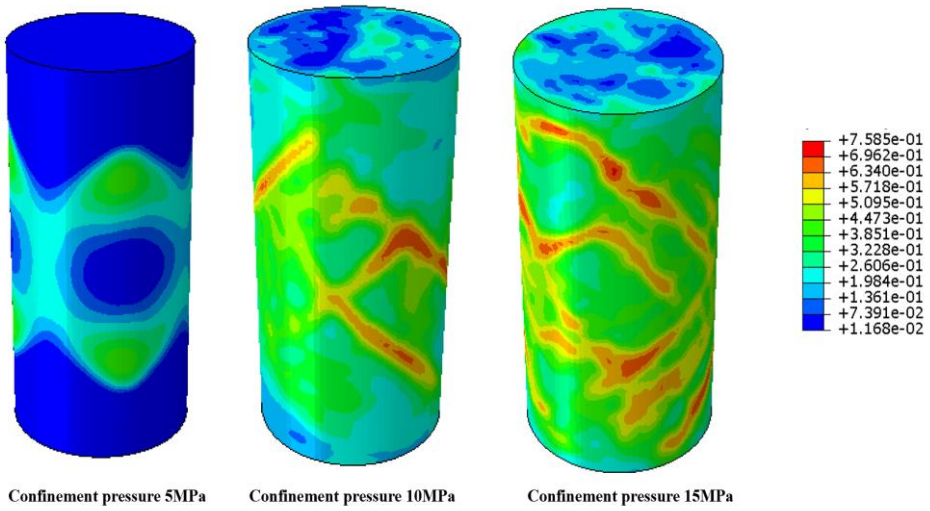

(d) Moderately weathered shale

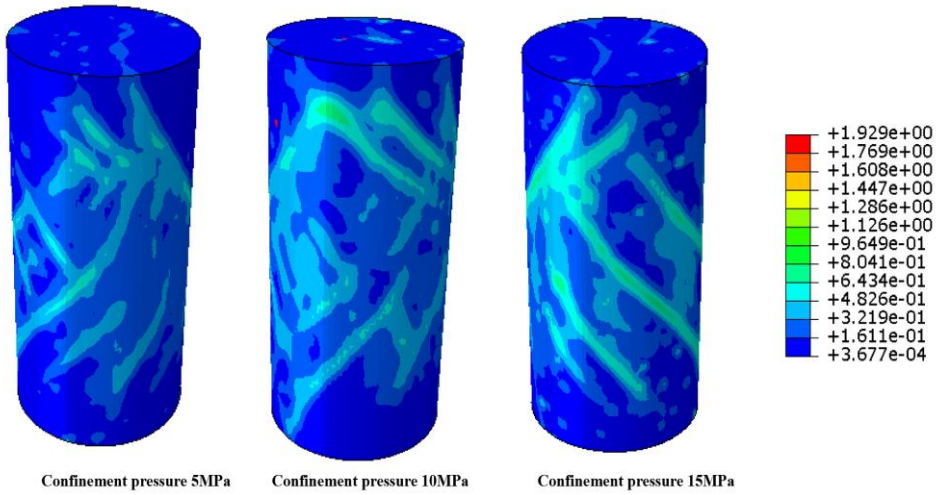

(e) Moderately weathered sandstone

Figure 6. Unit dissipative energy of rock samples under different confinement pressures

The degree of localization also shows clear lithology dependence. Granite and sandstone exhibit relatively sharp conjugate shear bands with high local dissipated energy, suggesting strong localization and limited post-peak deformation accommodation. Basalt, although locally more diffuse at low confinement, also develops well-defined high-energy bands at higher confinement, indicating that its failure remains strongly governed by elastic energy release once localization is triggered. By contrast, shale shows a wider and more continuous dissipation region, reflecting the stronger influence of weak cementation, bedding-related heterogeneity, and pre-existing microcrack closure–sliding processes, which permit a longer stage of distributed inelastic deformation before macroscopic instability. Limestone exhibits an intermediate behavior, with localization becoming more evident as confinement increases but remaining less concentrated than in basalt or sandstone. These differences are broadly consistent with the variation of the energy-density brittleness index B_{ED}. Rocks with higher B_{ED}, such as basalt and sandstone, tend to store more elastic energy before peak failure and dissipate less energy in a stable post-peak manner; accordingly, their damage is more prone to collapse into narrow, intense localization bands. In contrast, rocks with lower B_{ED}, particularly shale, exhibit more distributed dissipation and broader damage zones, indicating a relatively lower brittleness and a stronger capacity for post-peak energy consumption. The confinement-induced reduction in B_{ED} is likewise consistent with the observed widening of the dissipation zone, as higher confinement promotes a transition from strongly localized brittle rupture toward more spatially distributed damage evolution.

4.3. Normalized Dissipated Energy and Damage Evolution

Figure 7 presents the evolution of total energy density U, elastic strain energy density U_e, and dissipated energy density U_d with axial strain for five moderately weathered rocks under a confining pressure of 5 MPa. For all lithologies, U increases monotonically with strain, whereas the partitioning between U_e and U_d exhibits clear lithology dependence.

In the pre-peak stage, the response is predominantly governed by U_e: the curves of U and U_e nearly coincide, while U_d remains very small, indicating that most of the external work is stored reversibly in the rock skeleton and that irreversible damage is still limited. The main differences among lithologies do not appear in the early loading stage, but become progressively clearer in the near-peak and post-peak stages, when the competition between elastic energy storage and dissipation intensifies. For moderately weathered granite and shale (Figures 7-a and 7-d), U_e reaches a distinct maximum near the peak stress and then decreases, whereas the growth rate of U_d increases markedly after yielding and remains high in the post-peak stage. This indicates a clear transition from an energy-storage-dominated regime to a dissipation-dominated regime, reflecting sustained microcrack coalescence, frictional sliding, and progressive damage development after peak loading.

By contrast, for moderately weathered basalt, limestone, and sandstone (Figures 7b, 7c, and 7e), U and U_e remain almost coincident over most of the loading history, and U_d stays close to zero until failure is imminent. Even in the near-peak stage, the increase in U_d is relatively limited, suggesting that these rocks undergo little stable damage evolution before collapse and that their failure is controlled more strongly by elastic energy accumulation than by progressive dissipation. Therefore, the essential difference between the two lithology groups is concentrated mainly in the near-peak to post-peak stage: granite and shale exhibit a pronounced dissipation response after peak loading, whereas basalt, limestone, and sandstone retain an energy evolution pattern dominated by U_e, which is consistent with their relatively stronger brittleness under low confinement.

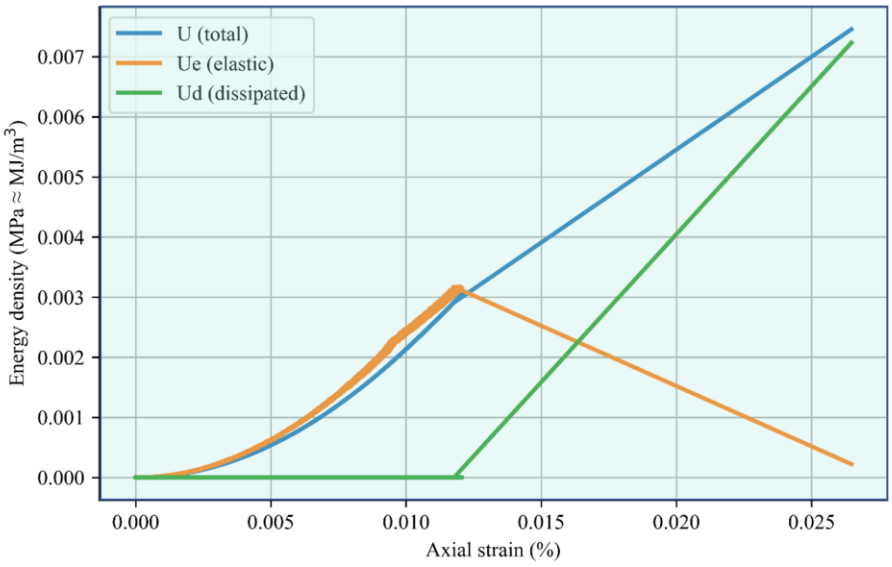

(a) Moderately weathered granite

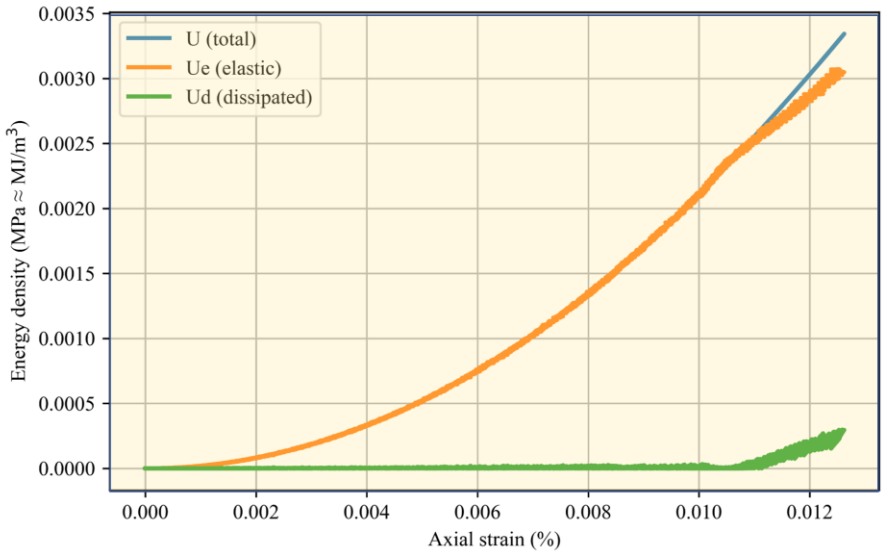

(b) Moderately weathered basalt

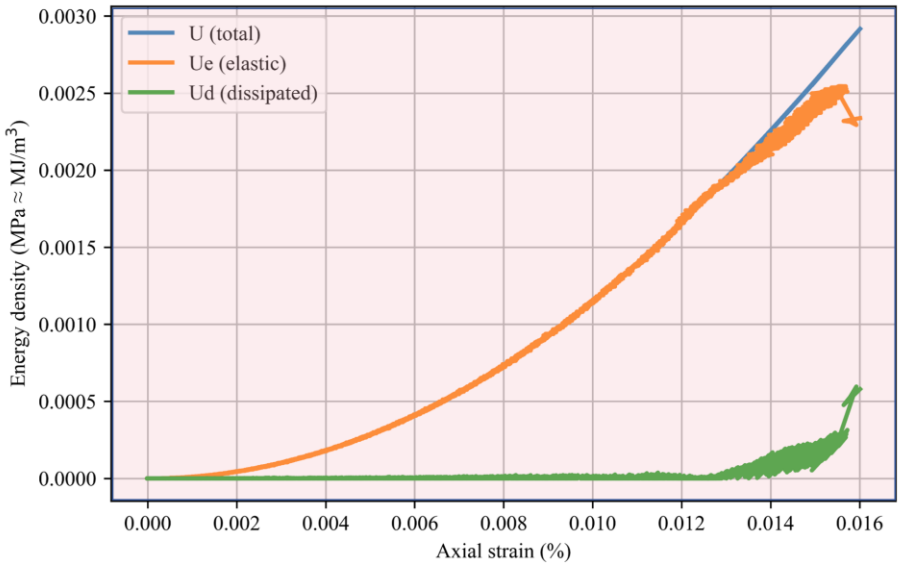

(c) Moderately weathered limestone

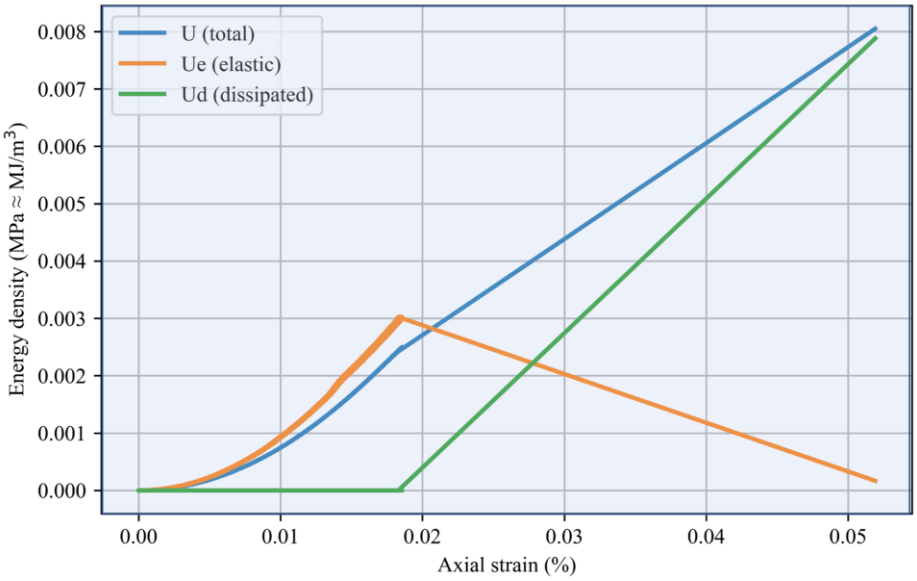

(d) Moderately weathered shale

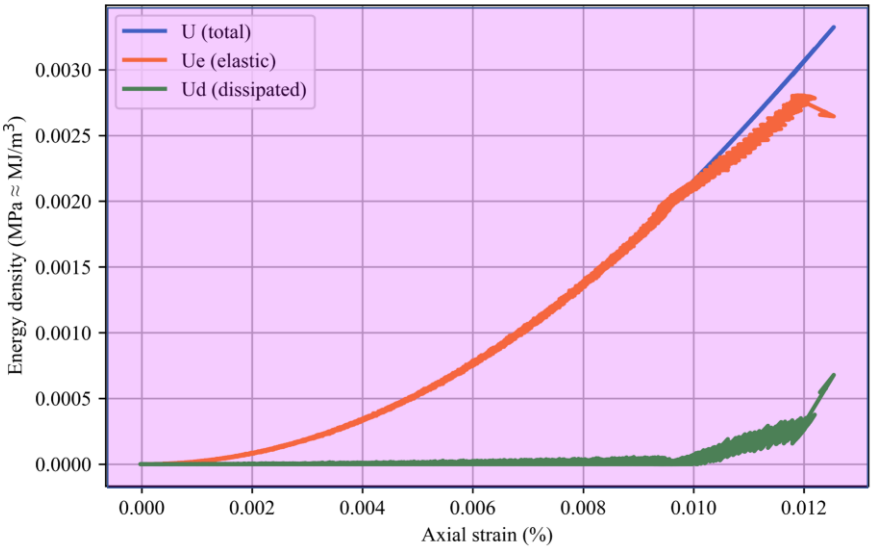

(e) Moderately weathered sandstone

Figure 7. Energy Densities of rock samples under a confining pressure of 5 MPa

Figure 8 presents a triangular radar plot of the energy-density brittleness index B_{ED} for five moderately weathered rock types under confining pressures of 5, 10, and 15 MPa. The three vertices correspond to the three confinement levels, and the concentric dashed triangles denote iso-values of B_{ED} from 0 to 1. For each lithology, the polygon defined by the three data points provides an integrated representation of both the absolute brittleness level and its sensitivity to confinement. A clear and consistent trend can be observed for all rocks: B_{ED} decreases as the confining pressure increases, indicating that higher confinement suppresses brittle instability and promotes a more ductile, energy-dissipative failure response. Mechanistically, this reduction in B_{ED} can be attributed to the fact that increasing confinement inhibits tensile crack opening, restrains dilation, and delays the formation of a dominant localization band. As a result, a greater proportion of the input work is consumed through stable microcrack propagation, frictional sliding, and distributed post-peak dissipation, while the relative contribution of abrupt elastic energy release becomes smaller. Since B_{ED} is designed to quantify the balance between pre-peak elastic energy accumulation and post-peak dissipation, the enhancement of confinement naturally shifts the response toward lower B_{ED} values.

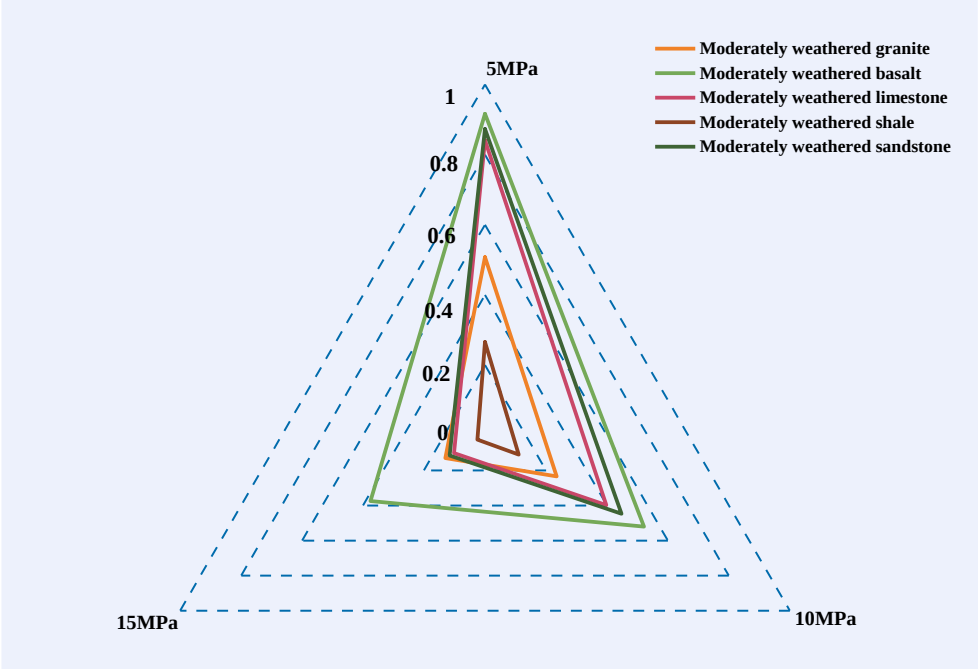

Figure 8. Energy-Density Brittleness Index B_{ED} of rock samples under different confinement pressures

The lithological ranking shown in Figure 8 is also physically meaningful. Basalt and sandstone consistently exhibit the highest B_{ED} values, indicating that they store a larger fraction of the input energy elastically prior to peak failure and dissipate relatively less energy in a stable post-peak manner. This is consistent with their relatively small peak strains, steeper post-peak stress drops, and stronger localization characteristics observed in Figures 5 to 7. Granite and limestone occupy an intermediate position, whereas shale shows the lowest B_{ED} values, reflecting its higher deformability and stronger capacity for sustained post-peak energy dissipation. In this sense, B_{ED} is well aligned with the traditional understanding of brittleness: rocks that fail abruptly with limited deformation accommodation and rapid stress degradation correspond to higher B_{ED}, whereas rocks with broader dissipation zones, larger peak strains, and more progressive post-peak damage correspond to lower B_{ED}. However, compared with conventional brittleness indices defined only from geometric features of the stress–strain curve, B_{ED} has a clearer physical basis because it explicitly incorporates both energy storage before peak and energy consumption after peak failure.

From an engineering perspective, the main advantage of B_{ED} is that it provides a scalar yet mechanistically meaningful indicator for brittleness assessment across different lithologies and confinement conditions. Unlike purely phenomenological indices, it can directly reflect the tendency of a rock mass either to release stored energy abruptly or to dissipate it progressively during failure. This makes B_{ED} particularly useful for excavation and support design in long tunnels. Rocks with high B_{ED}, such as basalt and sandstone, may require stronger confinement retention, more timely support installation, and closer monitoring of sudden brittle instability, whereas rocks with lower B_{ED}, such as shale, may permit a design strategy that pays greater attention to cumulative deformation and distributed damage evolution. Therefore, B_{ED} is not only effective for comparative brittleness evaluation, but also valuable for translating energy-based failure characteristics into practical engineering judgement and support decision-making.

5. Discussion

5.1. Performance of the Unified Energy-Based Framework

The numerical model reproduces the triaxial stress–strain curves and failure patterns of moderately weathered granite with good accuracy, which indicates that the adopted damage–plasticity law and energy decomposition are reasonable. On this basis, applying the same framework to basalt, limestone, shale and sandstone allows a consistent comparison of their energy-storage and dissipation behavior. Although the analysis of basalt, limestone, shale, and sandstone is conducted within the same constitutive and energetic framework using their respective mechanical parameter sets, and therefore has a reasonable basis for comparative applicability, full experimental validation across all lithologies remains to be completed. Compared with strength- or deformation-based indices, the separation of external work into total, elastic and dissipated energy captures the internal damage evolution more directly, while the normalized dissipated energy $\bar{U}_d$ and brittleness index B_{ED} provide scalar measures that can be compared across different rocks and confining pressures.

5.2. Lithology and Confinement Effects on Energy Dissipation

Results at 5 MPa show clear lithology-dependent patterns. Granite and shale exhibit a pronounced shift from elastic energy accumulation before the peak to rapid dissipated-energy growth after the peak, revealing strong post-peak damage development. Basalt, limestone and sandstone are dominated by elastic energy over most of the loading path, with only limited dissipation just before failure, which is characteristic of more brittle behavior. Spatial fields of unit dissipated energy confirm that granite and sandstone form well-defined shear bands, whereas basalt, limestone and shale display more distributed or confinement-sensitive dissipation zones.

Confining pressure generally reduces brittleness for all rocks. From 5 to 10 MPa, peak strength and peak strain increase, the dissipation zone enlarges, and B_{ED} decreases, indicating a transition towards more ductile, energy-dissipative failure. Although the 15 MPa simulations show an anomalous reduction in strength—likely related to modeling limitations rather than intrinsic behavior—the energy indices remain consistent: sudden failures with limited dissipation correspond to higher B_{ED}.

5.3. Engineering Implications for Tunnel Design

In the Jinmen Tunnel, moderately weathered rocks of different lithologies occur along the alignment under varying in-situ stresses. The present results suggest that zones dominated by basalt and sandstone, which have higher B_{ED}, are more prone to sudden, brittle failures once the accumulated elastic energy is released. These sections should therefore be supported early and stiffly, for example with dense rock bolts and shotcrete, to control rapid shear-band formation. Shale-rich zones, which show lower B_{ED} and higher dissipation capacity, are less likely to fail catastrophically but may deform more; support in these areas should focus on deformation control and long-term stiffness. Maintaining moderate confinement during excavation by using small advance rounds, pre-support and timely invert closure can shift the surrounding rock towards a lower-B_{ED} regime and improve tunnel stability.

5.4. Comparison with Previous Studies

The present results are broadly consistent with previous studies on rock brittleness, energy evolution, and confinement-dependent failure mechanisms. First, the observed decrease in brittleness with increasing confining pressure agrees well with the general trend reported in recent studies, which have shown that higher confinement suppresses tensile crack opening, restrains dilatancy, delays unstable crack coalescence, and promotes a more distributed and energy-dissipative failure process. In the present study, this effect is reflected by the increase in peak strength and peak strain, the widening of the high-dissipation zone, and the systematic reduction in the energy-density brittleness index B_{ED} as confinement increases from 5 to 10 MPa, indicating a transition from abrupt brittle rupture toward a relatively more stable deformation-and-dissipation regime. Second, the lithology-dependent energy partitioning obtained in this study is also in line with recent energy-based brittleness research, which emphasizes that rock brittleness is fundamentally governed by the competition between pre-peak elastic energy storage and post-peak irreversible dissipation.

The present results further show that granite and shale exhibit a more pronounced transition from elastic-energy accumulation to dissipation-dominated behavior near and after peak loading, whereas basalt, limestone, and sandstone remain largely dominated by elastic energy over most of the loading history and dissipate only a limited portion of the input work before collapse. These differences are also reflected in the spatial distribution of dissipated energy, where rocks with stronger brittleness tend to exhibit narrower and more intense localization bands, while less brittle rocks show broader and more distributed damage zones. Third, compared with conventional brittleness indicators based mainly on the geometric features of the stress–strain curve, the proposed B_{ED} index has a clearer physical basis because it directly characterizes the balance between pre-peak elastic energy accumulation and post-peak dissipation demand, thereby

reflecting more explicitly the intrinsic process of energy storage, release, and consumption during rock failure. In this sense, B_{ED} not only remains consistent with the traditional understanding of brittleness, namely limited deformation capacity and abrupt post-peak degradation, but also provides a more mechanistically grounded scalar parameter for comparing different lithologies and confinement conditions. This makes it particularly valuable for engineering applications, since it allows brittle failure tendency to be assessed from the perspective of energetic instability potential rather than solely from stress–strain morphology, and therefore offers a more physically meaningful basis for excavation control and support design in long tunnels such as the Jinmen Tunnel.

6. Conclusion

A unified three-dimensional numerical framework incorporating a coupled damage–plasticity constitutive model and energy decomposition was established to investigate the triaxial compression behavior of five moderately weathered rocks. The model was validated against the measured stress–strain curves and failure patterns of moderately weathered granite, demonstrating its ability to reproduce deformation, damage evolution, and brittle failure. The results show clear lithology-dependent differences in energy evolution. Granite and shale exhibit a pronounced transition from pre-peak elastic energy storage to rapid post-peak dissipation, whereas basalt, limestone, and sandstone remain dominated by elastic energy over most of the loading path and dissipate only a limited amount of energy before collapse. Increasing confining pressure generally reduces brittleness: from 5 to 10 MPa, the dissipation zone widens and the energy-density brittleness index B_{ED} decreases, indicating a shift toward a more ductile, energy-dissipative response. In terms of brittleness ranking, basalt and sandstone are the most brittle, granite and limestone show intermediate behavior, and shale is the least brittle.

The proposed B_{ED} has important theoretical significance because it links brittleness directly to the balance between pre-peak elastic energy accumulation and post-peak dissipation, thus capturing the physical essence of energy storage, release, and consumption more effectively than conventional stress–strain-based indices. For the Jinmen Tunnel and similar long tunnels, the results suggest that basalt- and sandstone-dominated sections require earlier and stiffer support to control sudden energy release and shear-band development, whereas shale-rich sections should place greater emphasis on deformation control. Nevertheless, the present study is limited to homogeneous specimens under quasi-static triaxial loading and does not explicitly consider structural discontinuities, cyclic or dynamic loading, or hydro-mechanical coupling. Future work should therefore extend the framework to heterogeneous rock masses and more complex loading environments, and further calibrate B_{ED} using broader laboratory and field datasets.

6.1. Limitations and Outlook

This study is based on a homogeneous and isotropic representation of each lithology, which provides a convenient unified framework but also introduces some limitations. In particular, this idealization may produce a smoother pre-peak stress–strain response and a more idealized post-peak instability pattern than those of natural moderately weathered rock masses. It may also affect the predicted localization behavior, since natural joints, bedding planes, and weak surfaces can alter the position, inclination, and width of shear bands, especially in shale and in fractured anticline zones. In addition, the proposed B_{ED} is more appropriate for relative comparison than for defining absolute brittleness thresholds directly applicable to field conditions. Future work should therefore incorporate structural discontinuities, material heterogeneity, and broader experimental datasets to improve the realism and engineering applicability of the proposed framework. In particular, future work will extend the experimental validation to additional moderately weathered lithologies, especially basalt, limestone, shale, and sandstone, by incorporating more triaxial test data to further assess and refine the general applicability of the proposed framework.

7. Declarations

7.1. Author Contributions

Conceptualization, K.W.; methodology, K.W.; formal analysis, E.Y.; investigation, L.L.; validation, L.L.; resources, L.L.; data curation, X.L.; writing—original draft preparation, E.Y.; writing—review and editing, X.L. and K.W. All authors have read and agreed to the published version of the manuscript.

7.2. Data Availability Statement

The data presented in this study are available on request from the corresponding author.

7.3. Funding

The authors received no financial support for the research, authorship, and/or publication of this article.

7.4. Conflicts of Interest

The authors declare no conflict of interest.

8. References

[1] Qiu, P. Q., Wang, W. W., Wang, K., Zhang, X. Q., Ning, J. G., Zhao, C. L., Jiang, Y. L., Zheng, J. D., Cai, T. T., & Yang, X. (2025). Experimental study on the energy dissipation mechanism of bolted rock under dynamic loading. Scientific Reports, 15(1). doi:10.1038/s41598-025-02436-7.

[2] Liu, G., Peng, Y., Zuo, Q., Su, Y., & Wu, L. (2022). Dynamic Mechanics and Energy Dissipation of Saturated Layered Phyllite. Minerals, 12(10), 1246. doi:10.3390/min12101246.

[3] Li, C., Mo, P. Q., & Li, S. C. (2024). Stability analysis of energy dissipation mechanisms in rocks surrounding circular opening. Applied Mathematical Modelling, 127, 327–342. doi:10.1016/j.apm.2023.11.020.

[4] Wang, C., Zuo, C., & Zhao, Z. (2023). Evolution Model of Coal Failure Using Energy Dissipation under Cyclic Loading/Unloading. Applied Sciences (Switzerland), 13(9), 5797. doi:10.3390/app13095797.

[5] Li, Y., Zhao, T., Li, Y., & Chen, Y. (2022). A five-parameter constitutive model for hysteresis shearing and energy dissipation of rock joints. International Journal of Mining Science and Technology, 32(4), 737–746. doi:10.1016/j.ijmst.2022.05.002.

[6] Liu, Z., Miao, S., Liang, M., Yang, P., Zhao, Z., & Chang, N. (2024). Characteristics and Association Mechanism of Energy Dissipation and Crack Development in Siltstone Under Triaxial Cyclic Loading and Unloading. Rock Mechanics and Rock Engineering, 57(12), 10399–10425. doi:10.1007/s00603-024-04098-9.

[7] Li, Y., Han, L., & Shang, T. (2024). Energy evolution and brittleness analysis of sandstone under confining pressure unloading. Rock Mechanics and Rock Engineering, 57(7), 4729-4754. doi:10.1007/s00603-024-03818-5.

[8] Kolesnikov, G., & Shekov, V. (2022). Energy Criterion for Fracture of Rocks and Rock-like Materials on the Descending Branch of the Load–Displacement Curve. Materials, 15(22), 7907. doi:10.3390/ma15227907.

[9] Wang, Z., Yang, Y., Xu, Y., Xin, C., Liang, P., & Guo, N. (2023). Analysis of Energy Evolution and Acoustic Emission Characteristics of Rocks under Cyclic Loading and Unloading. Applied Sciences (Switzerland), 13(18), 10453. doi:10.3390/app131810453.

[10] Long, Y., Sun, L., Cai, Z., Jiang, Z., Wang, Z., He, Q., & Bai, Z. (2023). Cyclic Loading and Unloading of Weakly Consolidated Sandstone with Various Water Contents. Sustainability (Switzerland), 15(18), 13866. doi:10.3390/su151813866.

[11] Wang, B., Zhu, J., Jin, Z., Xu, D., Zhu, Y., & Guo, Z. (2025). Energy dissipation and dilation processes of rock mass under incremental cyclic loading and unloading. Scientific Reports, 15(1), 17303. doi:10.1038/s41598-025-02146-0.

[12] Štambuk Cvitanović, N., Kavur, B., Vrkljan, I., & Miščević, P. (2025). The effects of test specimen shape tolerances on determining the mechanical and energy dissipation properties of limestone rock. Rudarsko Geolosko Naftni Zbornik, 40(3), 167–193. doi:10.17794/rgn.2025.3.12.

[13] Salyukov, V. S., Kutkin, Y. O., & Voznesenskii, A. S. (2025). Experimental Determination of Dissipation Factor in Rock Samples of Different Types and Genesis. Journal of Mining Science, 61(3), 356–364. doi:10.1134/S1062739125030020.

[14] Reches, Z., & Wetzler, N. (2025). Energy dissipation and fault dilation during intact-rock faulting. Journal of Structural Geology, 191, 105325. doi:10.1016/j.jsg.2024.105325.

[15] Shekov, V., & Kolesnikov, G. (2023). Differential Energy Criterion for Brittle Fracture: Conceptualization and Application to the Analysis of Axial and Lateral Deformation in Uniaxial Compression of Rocks. Materials, 16(13), 4875. doi:10.3390/ma16134875.

[16] Li, Y., Jia, D., Rui, Z., Peng, J., Fu, C., & Zhang, J. (2017). Evaluation method of rock brittleness based on statistical constitutive relations for rock damage. Journal of Petroleum Science and Engineering, 153, 123–132. doi:10.1016/j.petrol.2017.03.041.

[17] Guo, Y. P., Liu, D. Q., Yang, S. K., Wang, Y., Hu, Y., Zhang, X. P., ... & Li, Z. W. (2025). A new rock damage constitutive model based on usher function and its application to brittleness evaluation. Rock Mechanics and Rock Engineering, 58(2), 1451-1472. doi:10.1007/s00603-024-04248-z.

[18] Li, S., Kuang, Z., Qiu, S., & Zheng, H. (2022). Review of rock brittleness evaluation methods and discussion on their adaptabilities. Journal of Engineering Geology, 30(1), 59-70. doi:10.13544/j.cnki.jeg.2021-0677.

[19] Geng, K., Chai, J., Qin, Y., Xu, Z., Cao, J., Zhou, H., & Zhang, X. (2023). Damage evolution, brittleness and solidification mechanism of cement soil and alkali-activated slag soil. Journal of Materials Research and Technology, 25, 6039–6060. doi:10.1016/j.jmrt.2023.07.087.

[20] Liu, Z., Du, B., Zhu, H., Jiang, Y., Wang, T., Chen, W., Zhao, Y., & Wang, Y. (2026). Hydro-mechanical damage modeling of water-bearing sandstone using an energy dissipation approach under triaxial stress. Scientific Reports, 16(1), 1927. doi:10.1038/s41598-025-31740-5.

[21] Xiao, F., & Mo, R. (2025). Study on Creep Energy Dissipation and Damage Deformation Characteristics of Rock Under Unloading Confining Pressure. Rock Mechanics and Rock Engineering, 1-16. doi:10.1007/s00603-025-04781-5.

[22] Nguyen, N. T., Nguyen, G. D., Karakus, M., Bui, H. H., & Phan, D. G. (2025). Controlling behaviour of constitutive models for rocks using energy dissipations. International Journal of Plasticity, 184, 104196. doi:10.1016/j.ijplas.2024.104196.

[23] Le, V. T., Nguyen, T. V., Nguyen, N. T., Nguyen, G. D., Karakus, M., & Bui, H. H. (2025). A Simple 3D Damage-Plasticity Model with Energy-Based Regularisation in SPH for Modelling Fractured Quasi-brittle Rocks. Rock Mechanics and Rock Engineering, 58(9), 9937–9964. doi:10.1007/s00603-025-04638-x.

[24] Kovrizhnykh, A. M., Baryshnikov, V. D., & Khmelinin, A. P. (2025). Constitutive Equations for Creep, and Deformation- and Energy-Based Criteria of Rock Failure. Journal of Mining Science, 61(3), 345–355. doi:10.1134/S1062739125030019.